ENGINEERING

Scale-reconfigurable miniature ferrofluidic robots for negotiating sharply variable spaces

Xinjian Fan[1], Yihui Jiang[1], Mingtong Li[2], Yunfei Zhang[1], Chenyao Tian[3], Liyang Mao[3], Hui Xie[3], Lining Sun[1]*, Zhan Yang[1]*, Metin Sitti[2,4,5]*

Copyright © 2022 The Authors, some rights reserved; exclusive licensee American Association for the Advancement of Science. No claim to original U.S. Government Works. Distributed under a Creative Commons Attribution NonCommercial License 4.0 (CC BY-NC).

Magnetic miniature soft robots have shown great potential for facilitating biomedical applications by minimizing invasiveness and possible physical damage. However, researchers have mainly focused on fixed-size robots, with their active locomotion accessible only when the cross-sectional dimension of these confined spaces is comparable to that of the robot. Here, we realize the scale-reconfigurable miniature ferrofluidic robots (SMFRs) based on ferrofluid droplets and propose a series of control strategies for reconfiguring SMFR's scale and deformation to achieve trans-scale motion control by designing a multiscale magnetic miniature robot actuation (M^3RA) system. The results showed that SMFRs, varying from centimeters to a few micrometers, leveraged diverse capabilities, such as locomotion in structured environments, deformation to squeeze through gaps, and even reversible scale reconfiguration for navigating sharply variable spaces. A miniature robot system with these capabilities combined is promising to be applied in future wireless medical robots inside confined regions of the human body.

INTRODUCTION

Untethered magnetic miniature robots can navigate in lumina and tubular tissues, enabling new minimally invasive therapeutics and diagnostic medical procedures by shortening recovery times, decreasing the risk of infection, and reducing the possibility of complications (*1*–*5*). Therefore, magnetic miniature robots have undergone rapid development over the past 2 decades, owing to their potential applications in medicine and bioengineering (*6*–*8*). For example, previous works have proven that magnetic miniature robots can pass through the confined spaces inside the human body (e.g., tissue gaps and blood vessel branches) to realize micromanipulation and cargo delivery with cell-level precision (*9*, *10*), enabling active targeted treatments at the microscale (*11*, *12*). Recently, soft miniature robots made of active materials, such as fluids, gels, and elastomers, have demonstrated a relatively large number of degrees of freedom compared to rigid materials based on fixed shapes (*13*). In addition, various deformations of these robots can be addressed by programmable structures and magnetization profiles under an external magnetic field, highlighting their flexibility and applicability in unstructured environments (*13*–*15*).

In particular, the ferrofluid-based soft robots have emerged and advanced significantly, since they enable autonomous movement and deformation via the programming of external magnetic fields spatiotemporally through self-organized fluid dynamics rather than relying on the intricate and sophisticated solid structure design. Many research groups have explored the potential of ferrofluidic miniature robots and shown a series of interesting experimental results, as well as the mechanisms behind them (*16*–*25*). For instance, Latikka *et al.* (*17*) studied the magnetic field–induced splitting of ferrofluid droplets immersed in an immiscible liquid and discussed related dynamics and applications. Ahmed *et al.* (*18*) made notable progress in the study of locomotion, deformation, splitting/fusion, and potential applications of millimeter-scale ferrofluidic droplets. Nacev *et al.* (*19*) have demonstrated the medical application of ferrofluids. They designed and verified an original mechanism to optimally control multiple electromagnets in concert to move a single ferrofluid spot from the edge of a domain to a deep central target with minimal spreading.

However, despite recent advances in this field, the existing works have only focused on the characteristics and performances of miniature robots within the same scale without considering the matching degree of the robot's size and the scale of the workspace. For example, related studies have proven that the millimeter-scale robot can deliver drugs in large-scale confined spaces, such as stomach, intestines, and fallopian tubes in vivo (*26*–*29*). However, compared with the biological barriers, millimeter-scale robots are too large, limiting their ability to penetrate tumors and other tissues and decreasing their applicability to and practicality in targeted drug delivery. On the contrary, micrometer-scale robots have substantial maneuverability advantages because of their smaller size, enabling them to shuttle freely between tissue gaps and even through the blood-brain barrier. Therefore, micrometer-scale robots are the ideal solution to achieve accurate targeted drug delivery in vivo (*30*–*34*). Unfortunately, limited to their tiny volume, micrometer-scale robots are unable to reach sufficient levels to compete with diseased tissues, which are several orders of magnitude larger (*35*, *36*). Therefore, considering the inherent contradiction between reachability and the capability for specific-scale miniature robots, proposing soft miniature robots with reconfigurable scales and developing an actuation system compatible with multiscale robots could solve the aforementioned challenges.

Here, inspired by previous droplet-based miniature robots, we propose a series of control strategies for achieving trans-scale locomotion, deformation, and scale reconfiguration of miniature robots by using ferrofluid droplets as robots and designing an actuation system compatible with multiscale robots. The achievement of these trans-scale maneuvers via the present research is conceptualized as shown in Fig. 1. Considering the potential of ferrofluid droplets

[1]School of Mechanical and Electrical Engineering, Soochow University, No. 8, Jixue Road, Suzhou 215131, China. [2]Physical Intelligence Department, Max Planck Institute for Intelligent Systems, Heisenbergstr. 3, Stuttgart 70569, Germany. [3]State Key Laboratory of Robotics and Systems, Harbin Institute of Technology, Yikuang, Harbin 150080, China. [4]Institute for Biomedical Engineering, ETH Zürich, 8092 Zürich, Switzerland. [5]School of Medicine and College of Engineering, Koç University, 34450 Istanbul, Turkey.
*Corresponding author. Email: lnsun@hit.edu.cn (L.S.); yangzhan@suda.edu.cn (Z.Y.); sitti@is.mpg.de (M.S.)

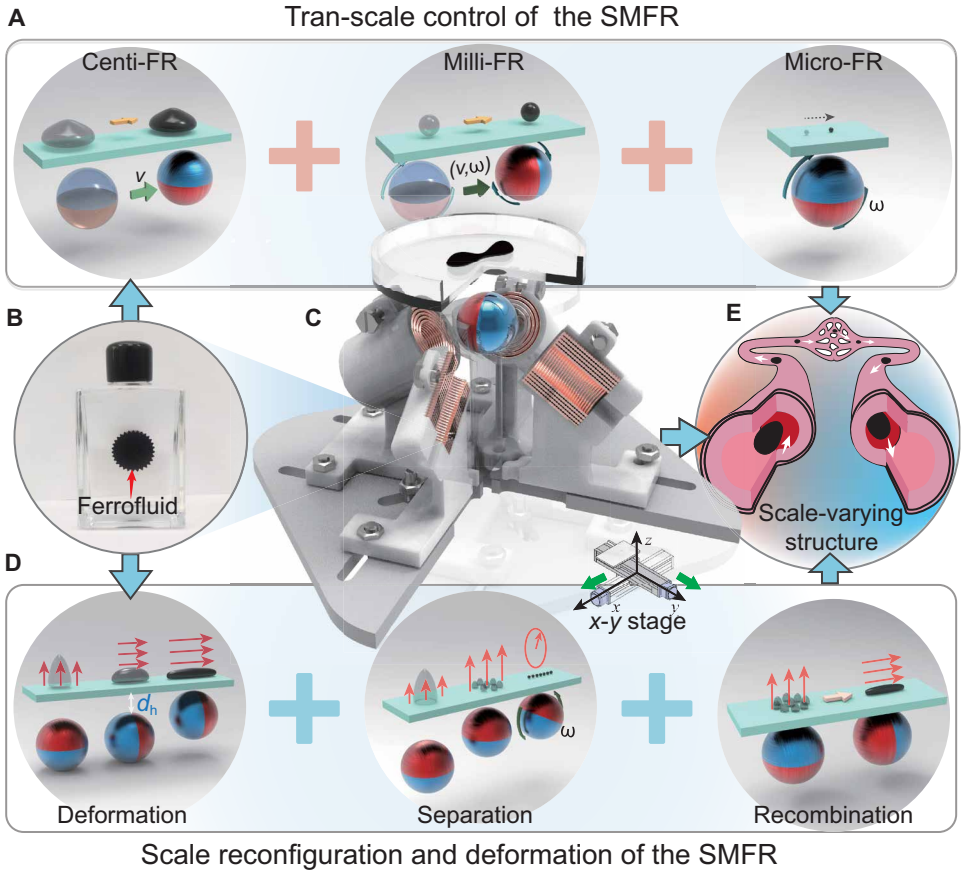

Fig. 1. Overview of trans-scale maneuver and scale reconfiguration strategies of the scale-reconfigurable miniature ferrofluidic robots (SMFRs). (**A**) Trans-scale control of the SMFR: locomotion of the centi-FR, milli-FR, and micro-FR based on magnetic gradient, both magnetic gradient and torque, and magnetic torque only, respectively. (**B**) Response behaviors of ferrofluid droplets in magnetic fields. (**C**) The SMFR is manipulated by a custom-designed magnetic actuation system (the M^3RA system) composed of four electromagnets, a spherical permanent magnet (SPM), and a motorized translation stage. To easily observe the internal composition of the system, we hide a quarter of the structure. (**D**) Deformation and scale reconfiguration of the SMFR: stretch deformation, scale-down through separation, and scale-up through recombination. The red arrow represents the polarization direction of the magnetic field. (**E**) Typical application scenario of the SMFR based on the combination of the above capacities: locomotion in a sharply variable space such as the vascular network.

(Fig. 1B) as miniature soft robots with extreme deformability, such as splitting and recombination, they are the best choice for the scale reconfiguration control research in this work. Therefore, ferrofluidic robots (divided on the basis of the largest feature size), including centimeter-scale ferrofluidic robots (centi-FRs), millimeter-scale ferrofluidic robots (milli-FRs), and microscale ferrofluidic robots (micro-FRs), are used as magnetic agents. In addition, as shown in Fig. 1C, we designed a hybrid magnetic actuation, the multiscale magnetic miniature robot actuation (M^3RA) system, by combining electric and permanent magnets in one system, enabling us to use a weak background magnetic field generated by electromagnetic coils to control a strong actuating magnetic field generated by the permanent magnet, which can generate a powerful magnetic field ($\boldsymbol{B}$)/gradient ($\nabla\boldsymbol{B}$) field simultaneously in a programmable way. On the basis of the M^3RA system, the shape and scale reconstruction and motion control of the scale-reconfigurable miniature ferrofluidic robot (SMFR) were well studied (Fig. 1, A and D), which enabled us to demonstrate the capabilities of SMFR by negotiating sharply variable environments with multiscale construct features (Fig. 1E). We envision that the SMFR's ability to realize combined locomotion, deformation, and scale reconfiguration could enable access to complex tight regions and indicates a great potential for practical use in laboratory-on-a-chip applications and biomedical procedures with minimal invasiveness and safe accessibility.

RESULTS

Characterization and actuation strategies of the SMFR

As shown in Fig. 2 (A and B), oil-based ferrofluid is a stable colloidal suspension of Fe_3O_4 nanoparticles (≈10 nm, superparamagnetic nanoparticle) dispersed in a surfactant and carrier liquid (light hydrocarbon oil) to prevent agglomeration, which exhibits a unique combination of liquid properties and strong magnetic response. That is, in the presence of an external magnetic field, the ferrofluid droplet tends to align with the magnetic field, producing an induced magnetic moment in the direction of the external magnetic field and minimizing the internal energy by changing its shape or position (*37*, *38*). However, it is worth noting that the ferrofluid is not a kind of typical magnetorheological fluid, where the diameter of the Fe_3O_4 particles is usually up to micrometer level (*39*), since it maintains an almost stable viscosity characteristic as the magnetic field intensity increases, as demonstrated in fig. S1A. Therefore, the fluid

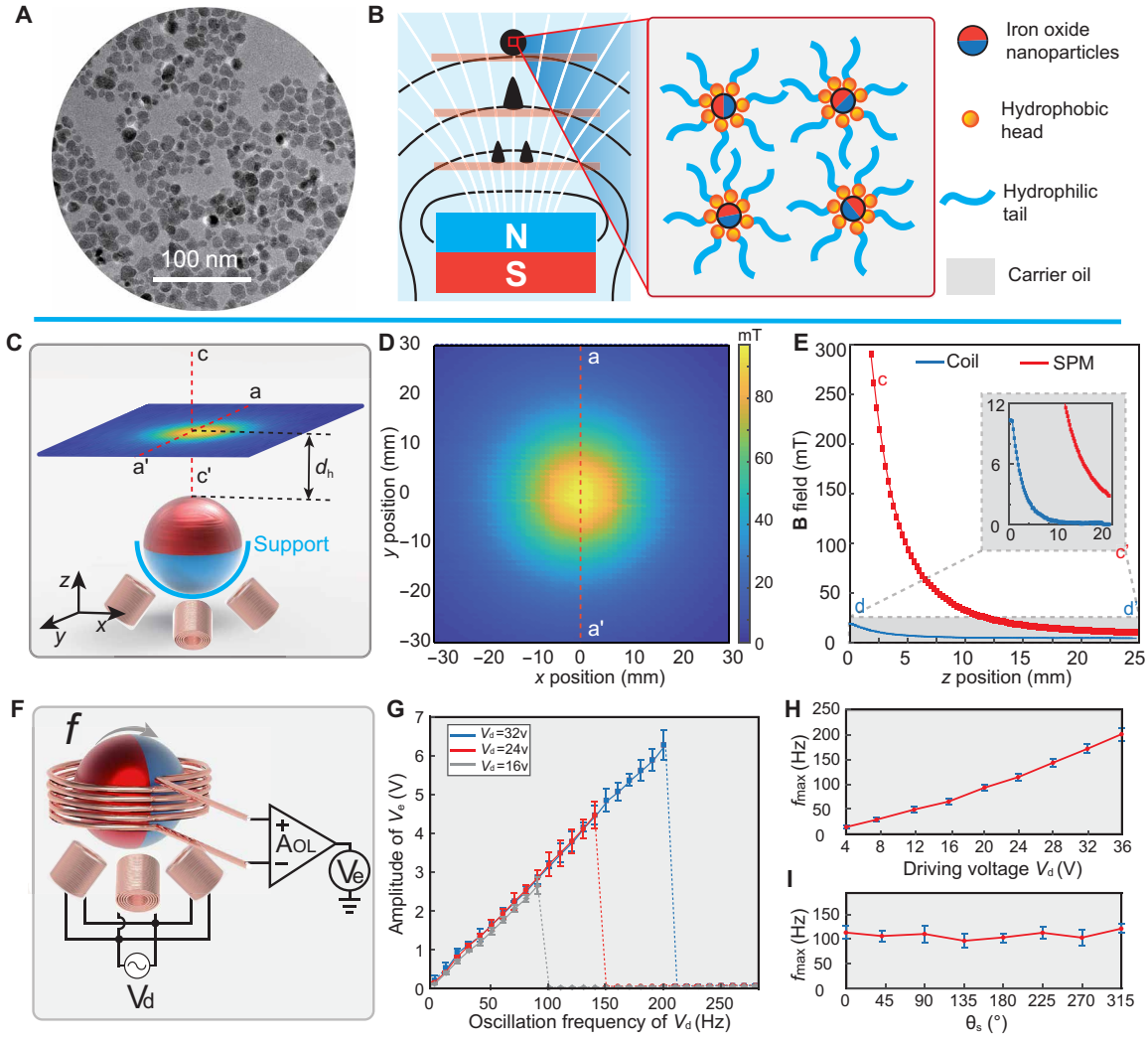

Fig. 2. Characterization of the SMFR and the M^{3}RA system. (**A**) The transmission electron microscopy (TEM) results of the nanoparticles in the ferrofluid. (**B**) The composition and magnetic response properties of the oil-based ferrofluid (white lines, magnetic field; black lines, constant field contours). (**C**) Magnetic field distribution and coordinate definition of the M^{3}RA system. (**D**) Measurement results of magnetic flux density $\boldsymbol{B}$ or equivalently the magnetic field $\boldsymbol{H} = \boldsymbol{B}/\mu_0$ distribution in the plane 5 mm from the top of SPM. (**E**) Comparison between the magnetic field generated by the coil (blue line) and the SPM along the polarization direction, with the subfigure showing the local enlarged drawing of the shaded part of the curve. (**F**) Schematic of the speed measurement setup of SPM based on the Faraday law of electromagnetic induction. (**G**) The relationship between the induced voltage V_e generated by cutting the magnetic induction line when SPM rotates and the amplitude V_d and the oscillation frequency of the driving voltage. Error bars represent the SDs for three times measurements. The maximum rotation frequency f_{max} of SPM as a function of the driving voltage V_d (**H**) and rotation angle θ_s when V_d = 20 V (**I**).

behavior of ferrofluid will maintain similar flexibility even under different magnetic flux densities. The competition between magnetic forces and the surface tension gives it elastomer-like properties, which allows the ferrofluid droplet as a whole to be manipulated. Moreover, since the flexibility and amorphousity of fluids are inherited, ferrofluid droplets have excellent deformability and even merging or splitting capabilities, easily enabling the study of the reconfiguration of their scales and making the SMFR a good candidate for studying the trans-scale control of miniature robots.

Ferrofluid droplets have been proven to be effectively actuated by a nonuniform magnetic field (*17*, *24*) or rotating magnetic field (*16*, *40*). The principle of actuating SMFRs by a nonuniform magnetic field is relatively simple. It mainly depends on the drag effect of magnetic gradient force, a volume force proportional to the size of the droplet. However, the mechanism behind the rotation of ferrofluid droplets with an external magnetic field is much more complicated. The magnetic particles in ferrofluids can be regarded as rigid magnetic dipoles (fig. S1B), which spin at the frequency of the external rotating magnetic field with a constant phase lag due to the viscous friction against the carrier liquid, and are equilibrated by the magnetic torque (*41*). Inside the SMFR, the corotation of two neighboring particles is dissipated by viscous friction; therefore, only at the interface is the friction low, and the SMFR's interface can rotate (fig. S1B). In short, this is a kind of rotation caused by the surface effect. Therefore, the larger the specific surface area (the smaller the size) of the SMFR, the higher the actuating efficiency, and vice versa. To verify this, we studied the maximum rotating speed of an SMFR with various scales in a rotating magnetic field

($\boldsymbol{B}$ = 2.5 mT) by measuring their maximum translation speeds on the substrate and comparing the magnitude of magnetic gradient forces on them (fig. S1C). The results show that a smaller-scale SMFR has a higher rotation speed but a weaker magnetic gradient force; in contrast, a larger-scale SMFR is subjected to a more notable gradient force, but its rotation ability is relatively diluted, which is consistent with the above analysis.

In conclusion, magnetic gradient force and magnetic torque affect the motion behaviors of SMFRs with different sizes at contingent levels; that is, smaller SMFRs are more susceptible to magnetic torque, as their magnetic gradient forces are ignorable (see note S3 for details). However, with the increase in the robot scale, the optimal actuation force gradually transits from magnetic torque to magnetic gradient force. Therefore, the micro-FR is preferable for actuation in a rolling manner by magnetic torque because of its unique torque-selective sensitivity. Centi-FR is easier to pull by suffering a powerful magnetic gradient force. As for milli-FR, it may be actuated by magnetic gradient force, torque, or more effectively by both.

The M^{3}RA system for actuating the SMFR

According to the previous inference, the key to achieving efficient control of the SMFR is a time-varying magnetic field with a powerful gradient force and torque. To tackle this challenge, we designed a hybrid magnetic actuator by integrating permanent magnet and electromagnets to create the M^{3}RA system, which has high compactness. As shown in Fig. 1C and fig. S2, four orthogonal solenoids are arranged inside this system at each bottom vertex of the cubic space, each pointing to the center where a spherical permanent magnet (SPM) composed of NdFeB exists. A goblet-like support was used to restrict the SPM's position, making its center always located at the focus of the four electromagnetic coil's axes. Besides, to reduce the friction between the SPM and the support, we coated their contact surfaces with low-viscosity lubricating oil and graphite powder, as shown in fig. S2B. A three-axis motorized translation stage was used to increase the system's flexibility and enable the programmability of magnetic fields in a wide range of available spaces (fig. S2C). The optimized parameters used for our machine prototype design are shown in note S2 (table S1).

Benefitting from its unique structure, the M^{3}RA system can generate a background magnetic field ($\boldsymbol{B}_b$) with customized directions by configuring the current inside the solenoid. According to Eq. 2 (see Materials and Methods), the magnetic moment $\boldsymbol{m}$ of SPM will be forced to align with $\boldsymbol{B}_b$ due to the existing magnetic torque between them. Therefore, the requisite magnetic field can be obtained by adjusting the position and/or orientation of the permanent magnet. Specifically, for a dynamic rotating field, the SPM will follow the field with a fixed misalignment angle ($\leq$90°); for a time-invariant magnetic field, it tends to align with the field. In this way, we realized the free control of an extremely strong actuation magnetic field $\boldsymbol{B}_a$ by a very weak magnetic field $\boldsymbol{B}_b$.

Figure 2 (C and D) illustrates the magnetic field ($\boldsymbol{B}_a$) distribution at a plane 5 mm (d_h) from the SPM's surface. For comparison, the corresponding results of the $\boldsymbol{B}_b$ generated by a coil of the M^{3}RA system were simulated and measured (fig. S3). Figure 2E shows the attenuation curves of $\boldsymbol{B}_a$ and $\boldsymbol{B}_b$ along the magnetization direction of the SPM and a coil, respectively. Combined with the experimental and simulation results in fig. S3, it is reasonable to conclude that the SPM could provide a more powerful static magnetic field $\boldsymbol{B}_a$ with an available magnetic field strength up to 300 mT and the highest magnetic gradient exceeding 50 T/m, which is much higher than the maximum background magnetic field $\boldsymbol{B}_b$ with corresponding parameters being 15 mT and 1.5 T/m on the top surface of the coil. It is worth noting that most of our later experiments can be implemented in a workplace far away from the SPM (d_h = 10 to 20 mm), where $\boldsymbol{B}_a$ can still reach 30 mT or 2 T/m.

In addition, the dynamic response capability of the M^{3}RA system is also a critical factor in realizing the trans-scale control of miniature robots. When actuated by a rotating background, the magnetic field is expressed as $\mathbf{B}_b(t) = B_b[\cos(\omega t)\mathbf{e}_x - \sin(\omega t)\mathbf{e}_z]$ on the (x, z) plane, and the SPM will rotate around the y axis with a mean angular velocity of ω because of the magnetic torque. The dynamic performance of the system can be measured on the basis of the Faraday law of electromagnetic induction by the homemade setup (Fig. 2F). Figure 2G shows the results obtained from studies on the evolution process of the angular frequency ω using a method as illustrated in fig. S4. The experimental results showed that when ω was below a specific frequency ω_c, the SPM followed the rotating background magnetic field synchronously; however, when $\omega > \omega_c$, the SPM no longer kept up with the rotating magnetic field and stopped abruptly. Usually, the ω_c is called the cutoff/critical frequency. Further analysis, as demonstrated in Fig. 2H, shows a very substantial linearity change of the cutoff frequency ω_c when varying the driving voltage V_coil of the background magnetic field. Notably, when the maximum driving voltage of the M^{3}RA system was up to 32 V, the cutoff frequency of the SPM reached an astonishing 200 Hz, with the energy consumed by the system being only about 10 W (one coil), which is hard to realize by the existing device because of bandwidth limitations or inertia confine (*42*). The next section of the survey is concerned with the isotropic factor and robustness of SPM's motion performance by measuring the ω_c of SPM when rotating in different directions (θ_s is defined in fig. S5) when driving by the same V_coil. The results (Fig. 2I) showed good consistency for the maximum rotating speed of the SPM in all directions despite some minor fluctuations due to the bottom support with uneven smoothness, which demonstrated its excellent controllability and repeatability.

Controlled deformation of the SMFR

Similar to water droplets in nature, the SMFR can passively fit the surrounding environment by maintaining the same shape as the container. Because of its unique magnetic responsiveness, the SMFR is capable of active deformability through programming the distribution of the external magnetic field (*43*). For example, when a horizontal polarized magnetic field is applied, the SMFR is stretched to reach an equilibrium state along with the orientation of the external field, owing to the competition between its internal magnetic forces and surface tension (Fig. 3A). It is well known that the inner magnetic forces acting on the ferrofluidic droplet can be expressed by the Maxwell stress tensor, denoted as τ_max, and is given as (*44*): $\tau_\mathrm{max} = -\mu B^2\boldsymbol{I}/2 + \mu\boldsymbol{BB}$, where μ is the permeability of the ferrofluids. $\boldsymbol{I}$ represents the unit matrix. The first term on the right-hand side contains the surface force, which is the source of the elongated stretch. In this case, the deformation of the SMFR can be characterized by the magnetic Bond numbers (*45*) as

$$\beta_0 = \mu_0 B^2 r_0/2\sigma \quad (1)$$

where σ is the surface tension coefficient, μ_0 is the permeability of the vacuum, and r_0 is the radius of the SMFR in zero fields. The β_0

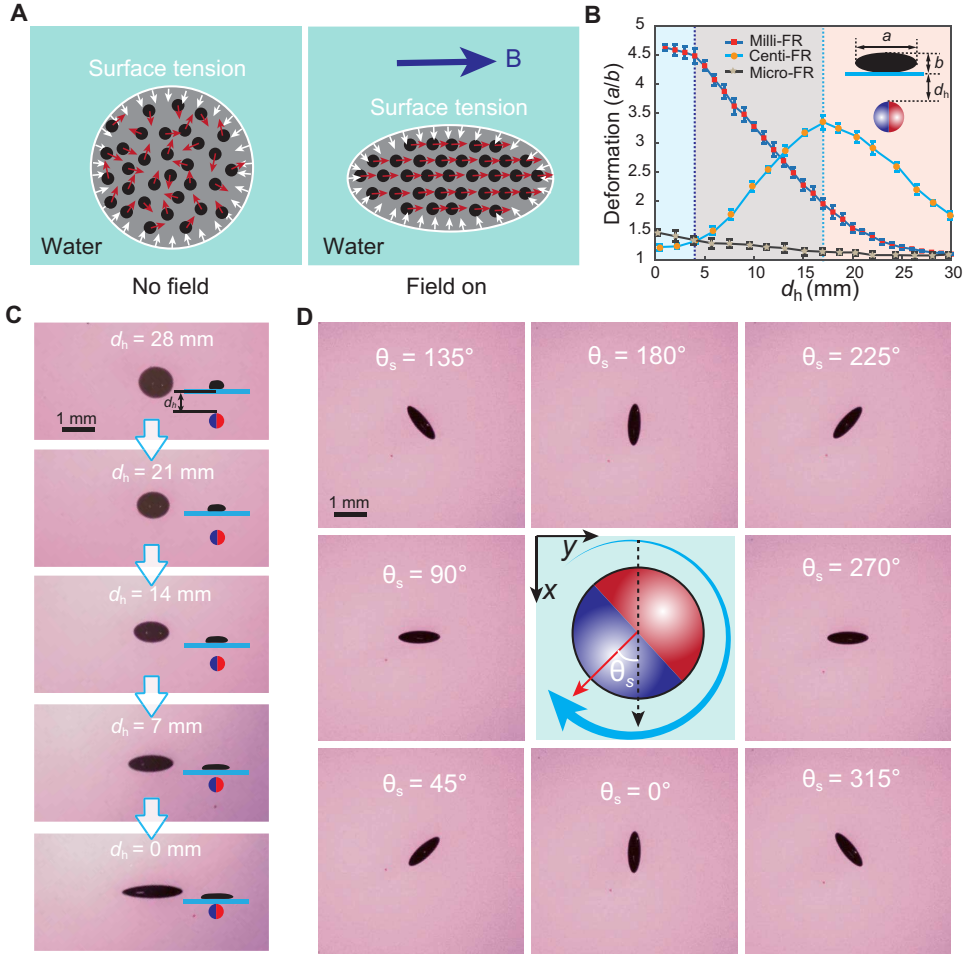

Fig. 3. Controllable deformation magnitude and direction of the SMFR. (**A**) Two-dimensional (2D) schematics of the stretch mechanism of the SMFR under the action of an external magnetic field. The red and blue arrows indicate the polarization direction of the internal magnetic particles and the external magnetic field, respectively. (**B**) The deformation of SMFRs (≈10-, 1-, and 0.05-mm diameter, respectively) as a function of the distance between the robot and the upper surface of the SPM. The deformation here is defined as the relative length ratio (a/b) between the long and short axis of the SMFR. (**C**) Deformation magnitude control of a milli-FR. The schematic diagrams in the right corner illustrate the relative position of SPM during the process in a side view. (**D**) Stretch angle control of a milli-FR.

can characterize the shape change of an SMFR: The smaller the β_0, the more spherical the SMFR will be. Therefore, in line with common expectations, more significant elongations will result from larger droplets or stronger field strengths.

As was demonstrated earlier, the M^{3}RA system can generate a customized magnetic field by adjusting the position and/or orientation of the SPM, which means the stretch direction and magnitude of the SMFR can be well controlled through regulating the orientation of the SPM and the distance between the SPM and SMFR (d_h), respectively. Here, the magnitude of the stretch is represented by the ratio (a/b) of the long axis (a) and the short axis (b). Figure 3B shows the deformability of SMFRs varying from the micrometer to centimeter scale as a function of d_h. It is apparent from the collected results that, limited to the smaller size, the micro-FR is capable of only slight deformability compared to the milli-FR, which can stretch to more than a fourth of its initial radius. Furthermore, it is worth noting that the centi-FR does not have the greatest deformability but is somewhere in between the best and worst. This is because as the volume of SMFR increases, it is more obviously affected by the magnetic field gradient force, which forces the ferrofluid to be enriched near the SPM. In addition, eq. S2 (see note S3) reveals the faster decrease in the field gradient as a result of distance rather than field intensity. Therefore, degenerate deformability occurs only when the robot is close enough to the SPM, which also explains why during the first half of the curves, the magnetic intensity is stronger, but the SMFRs are less likely to deform. As a demonstration, Fig. 3C (movie S1) shows that the deformation magnitude of a milli-FR can be well controlled by tuning the d_h. Except for the magnetic field strength, the nanoparticle content will also strongly affect the SMFR's magnetic deformability. Figure S6A shows that the deformability of SMFRs is a function of their magnetic nanoparticle content, indicating a positive correlation between them: The higher the concentration of magnetic nanoparticles, the stronger the deformability and magnetic responsiveness of the SMFRs. According to the experimental results, when the weight percentage of nanoparticles is less than 20%, the SMFR becomes insensitive to the magnetic fields with only slight deformation ($a/b < 2$) in our system. Furthermore, controlling the deformation direction of the SMFR is also of

great significance to enable it to pass through specially oriented narrow gaps. For example, Fig. 3D and movie S1 demonstrate that the stretch direction of a milli-FR can be indirectly regulated by adjusting the orientation of the SPM through spatiotemporal programming of the magnetic field. The performance of the stretch angle control is shown in fig. S6B: the average and maximum error over all angle measurements during this experiment are 1.32° and 5.7°, respectively, which is comparable to previous work where only electromagnetic force was used as the actuation system (*18*).

Locomotion of the SMFR

As discussed earlier, microscale magnetic robots are more sensitive to magnetic torque than magnetic force. Therefore, it is more efficient to actuate these robots in a rolling mode using a rotating magnetic field. In this case, the micro-FR always tends to follow a rotating magnetic field with a mean angular velocity of ω^{FR}. Once closed to the substrate, the apparent viscosity of the portion facing the solid surface increased, enabling the micro-FR to become a surface walker with a mean translation velocity v (Fig. 4Ai). Similar to the SPM in a rotating background magnetic field, the rotating speed of the micro-FR increases linearly and monotonously with the ascending frequency of the actuation magnetic field until it exceeds the cutoff frequency ω_c^{FR}.

On the basis of the above experiment and analysis results, the velocity and position of the micro-FR can be accurately controlled to track sophisticated paths. However, before that, we must first eliminate the influence of the magnetic gradient force. More specifically, although the magnetic gradient force cannot yield the efficient actuation of the micro-FR, it can affect its motion trajectory cumulatively. Consequently, there is often a static error δ_d for an open-loop

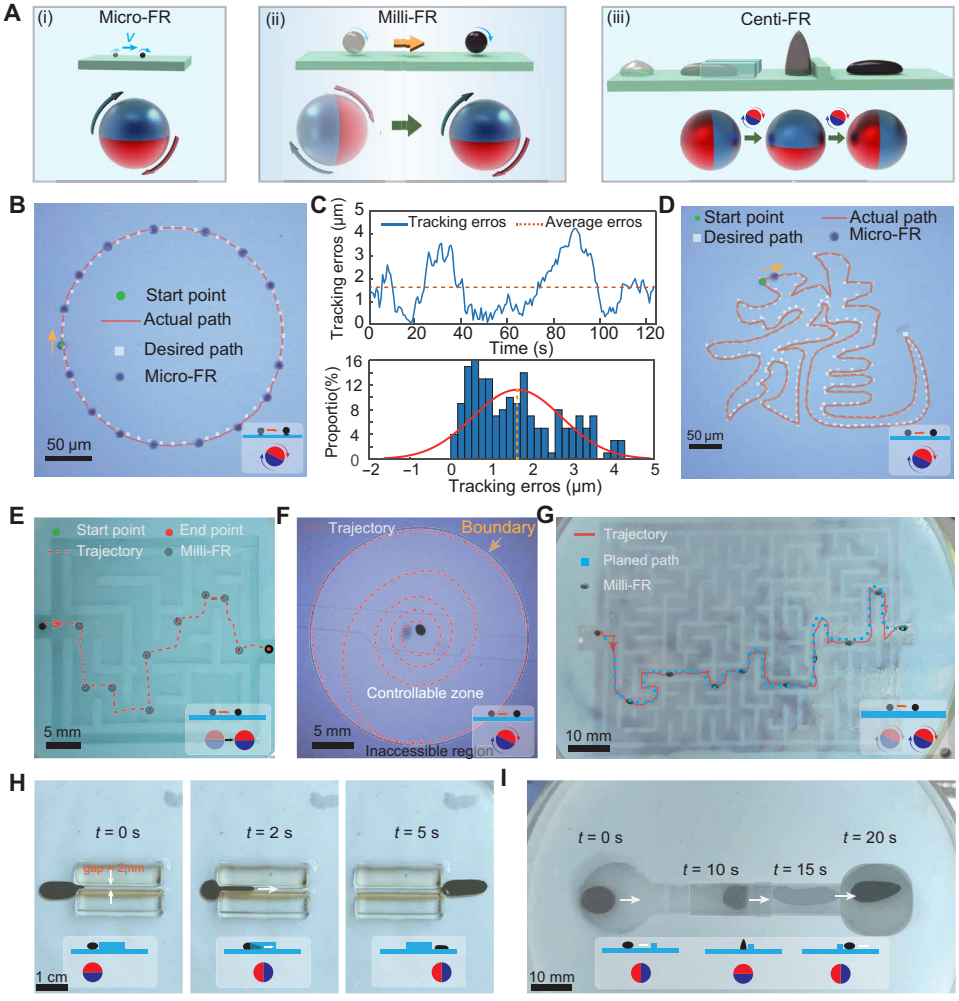

Fig. 4. Locomotion of milli-FR and centi-FR in complex and structured environments. (**A**) Trans-scale control schematics of SMFRs. (i to iii) Schematics of the magnetic actuation principle of the micro-FR, milli-FR, and centi-FR, respectively. (**B**) A micro-FR is actuated to follow a circular path in a closed-loop control manner. (**C**) Tracking results (upper) and distribution histogram of the tracking error (below) in (B). (**D**) Experimental results of tracking a sophisticated Chinese character–like path by a micro-FR. (**E**) The milli-FR is actuated by magnetic drag force to navigate a maze with meandering structures. (**F**) The milli-FR is actuated by a rotating magnetic field to move along a spiral trajectory. The highlighted circular area in this figure is the controllable and reachable range for SMFR, beyond which the milli-FR cannot access. (**G**) A milli-FR is actuated by the combination of magnetic force and torque. (**H**) A centi-FR is capable of crossing a narrow gap through reorientating and relocalizing the SPM simultaneously. (**I**) Overlapped sequential snapshots of a video, when a centi-FR is actuated to cross a channel with convex structures under the action of deformation and magnetic gradient force.

controller. As shown in fig. S7 (A, C, and D), compared to the first loop, the tracking trajectory of the second loop has obvious drifts with more substantial average tracking error and error ranges (measured by Euclidean distance). To tackle this tricky aporia, as illustrated in fig. S8, a vision-based closed-loop controller was introduced here. Figure 4 (B and C) and fig. S7B show that the motion trajectories and error analysis of a micro-FR when tracking a circular path with a closed-loop controller, which by contrast are more accurate and reproducible. On the basis of these improvements and perfections, the micro-FR is capable of tracking more sophisticated trajectories quickly and precisely. As shown in Fig. 4D and movie S2, a micro-FR with 10-μm diameter draws a traditional Chinese character–like trajectory at a speed of ≈5 μm/s. The means and SDs of the tracking results are shown in fig. S9. Although these paths are challenging due to their extreme curvatures and complex shapes, the robot could still stably follow them with a path deviation error within 0.2 ± 0.152 of the body length.

Turning now to the experimental evidence on milli-FR, the situation differs. Earlier analysis showed that, with the increase in the diameter of SMFRs, the efficiency of its rotation through magnetic torque is lowered, resulting in a small ω_c^{FR}. From another point of view, the increasing size makes the volumetric force suffered by the milli-FR more obvious and enables it to be operable by magnetic gradient force. In any case, the milli-FR can be actuated by both magnetic torque and magnetic gradient force, as illustrated by the schematics in Fig. 4Aii. Figure 4 (E and F) (see movie S3) shows that a milli-FR (≈1.5 mm) is controlled to cross a maze or follow a spiral path under the action of magnetic gradient force or magnetic torque, respectively. However, we found in experiments that the actuation method based solely on magnetic gradient force requires a small actuation distance d_h (<8 mm in our system). Otherwise, it usually causes failure; as for the actuation method based solely on magnetic torque (when the motor-based stage is locked), although it enables a more considerable actuation distance ($d_a \approx 25$ mm), the reachable area of the robot is limited to ≈30 mm, the outermost of the spiral line in Fig. 4F.

To address these constraints, we propose a method to actuate the milli-FR efficiently with an extensive range by using magnetic force and magnetic torque simultaneously based on the M^3RA system (Fig. 4Aii). As shown in Fig. 4G and movie S3, we steered the milli-FR navigation in a hydrogel maze with an actuation distance $d_a = 25$ mm. For comparison, we first used the magnetic force to drag the milli-FR along the planned trajectory by adjusting the position of the SPM below. However, the milli-FR fell behind the SPM quickly because of the severely attenuated magnetic gradient force and friction from the substrate. In the second attempt, we rotated the SPM and moved simultaneously while using a PID (proportional integral derivative) controller to control the translation direction of the milli-FR and another PID controller to adjust the position of the SPM by translating the *x*-*y* stage, ensuring that the milli-FR was always located in a proper scope. In this way, the milli-FR can pass through the large complex maze more smoothly, with the average and maximum path error in the overall experiments being only 1.2 and 3 mm, respectively. There were consistent deviations from the path, which may have been due to the momentum that the robot picked up, as it accelerated during certain parts of the track. Other possible explanations may include the heterogeneous flatness of the maze and the boundary effect when the milli-FR approached the maze wall.

The centi-FR had the lowest actuation efficiency by a rotating magnetic field, and its droplet-like shape was easily destroyed by a dynamic magnetic field (*46*). Therefore, it is not preferable to actuate the centi-FR using magnetic torque. In contrast, as discussed earlier, a large volume always results in a massive magnetic force, which indicates that magnetic gradient force enables the more efficient motion control of centi-FRs. Therefore, we can use the drag effect of the magnetic gradient force and the shape-shifting effect of the magnetic torque to realize the navigation of a centi-FR in unstructured environments (Fig. 4Aiii). As shown in Fig. 4H and movie S4, by simultaneously programming the orientation and position of the SPM, a typical centi-FR (≈10 mm diameter) can be made to deform and fill the narrow channel and then squeeze through the gap (≈2 mm width) under the drag of the magnetic gradient force. Besides, by reorientating and relocalizing the SPM, the centi-FR is endowed with obstacle surmounting ability. As shown in Fig. 4I and movie S4, when encountering a convex barrier, the orientation of the SPM was adjusted to point vertically (standing state), which resulted in a vertical deformation of the centi-FR with the overall height being much higher than the obstacles. In this case, once the SPM was restored to the lying state while advancing, the centi-FR overcame the obstacles. Our experimental results show that the centi-FR can cross barriers up to 2.5 mm high that cannot be overcome just through magnetic gradient force (see fig. S10 and movie S4). Those abilities potentially enable the controllable locomotion of centi-FR on rugged surfaces, such as the human intestine and stomach cavity.

Scale reconfiguration of the SMFR

According to Eq. 1 (see Materials and Methods), the deformability of the ferrofluid droplets mainly depends on both the surface tension and the magnetic field strength. Therefore, when encountering submillimeter or micrometer-scale confined spaces, surface tension of the SMFR dominates its shape and only enables weak deformability, which blocks it from squeezing through such channels. In this case, splitting the SMFR into smaller ones is a better choice. Thanks to their fluid nature, ferrofluid droplets are capable of splitting and merging, which enables their reversible scale reconfigurability. As illustrated in Fig. 5A, when a magnetic field is vertically applied from the bottom of a centi-FR, the combination of the high magnetic intensity and vertical gradient creates repulsive forces among the inner parts of the centi-FR, causing them to move away from each other until they tear the centi-FR apart (*25*). Therefore, the centi-FR can be divided into multiple milli-FRs by decreasing the d_h while maintaining the SPM a standing state. Once the magnetization direction of the SPM is rotated in the vertical plane, the resulting milli-FR can be combined into a centi-FR again, as illustrated in the right corners of Fig. 5C (movie S5), where the magnetic forces between the milli-FR make them align, collide, and merge into a centi-FR. Besides, to independently control the resulting daughter SMFRs after splitting a big one, we proposed a reliable separation method for them by integrating a tiny magnetic sphere, since the milli-FR can be driven by the magnetic gradient, which is easy to obtain even within a millimeter-scale space (*47*), therefore enabling us an efficient mechanism to lock and individually manipulate a designated milli-FR. Figure S11A illustrates the principles of generation and addressable control strategy of milli-FRs. First, the SPM approaches the centi-FR vertically to split it into multiple milli-FRs. Then, the SPM backtracks to the initial position, while the resulting

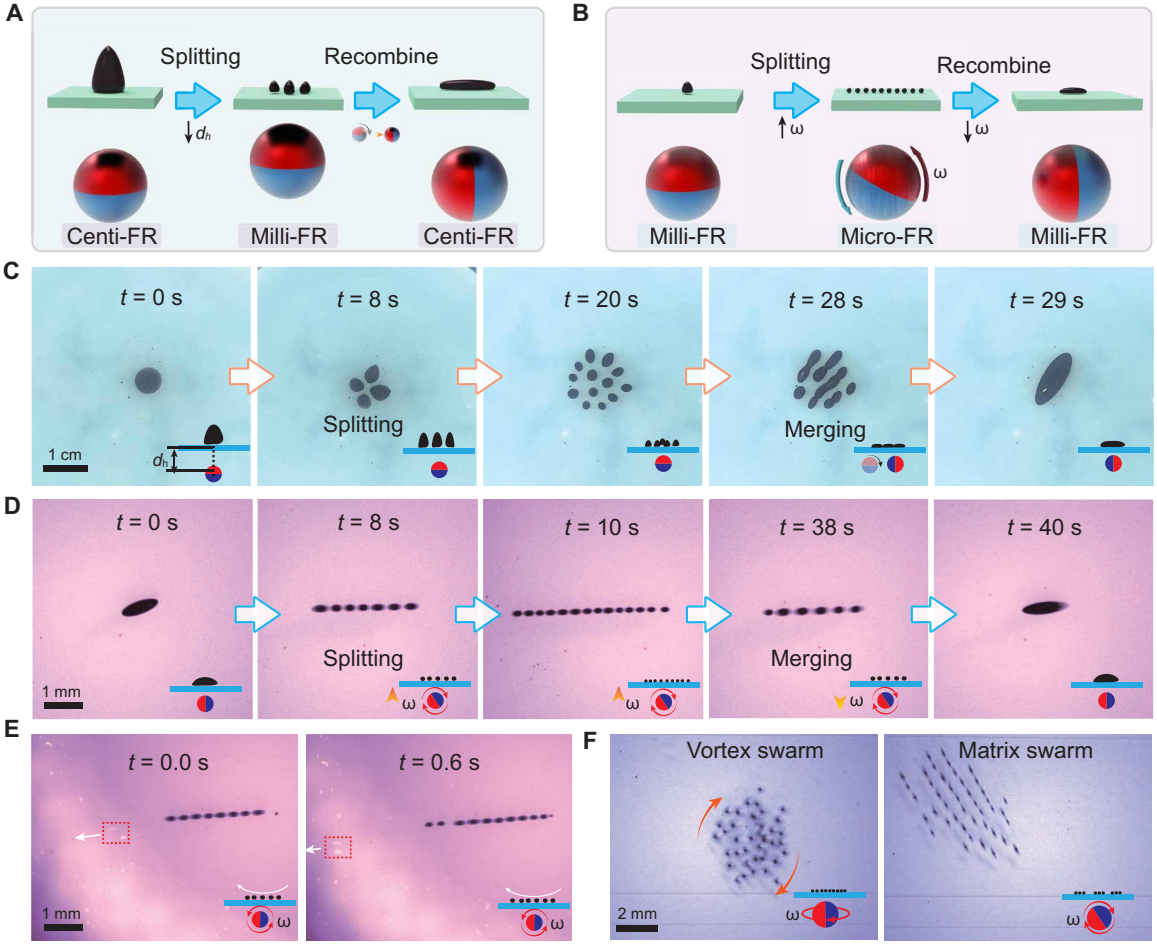

Fig. 5. Scale reconfiguration of the SMFR through splitting or merging. (**A**) Schematics of a centi-FR splitting into milli-FRs and recombination by tuning the position and orientation of the SPM. (**B**) Schematics of a milli-FR splitting into micro-FRs and recombination by adjusting the rotation frequency of the SPM. (**C**) Image sequences show the experimental splitting process (scale down to milli-FR) of the centi-FR when the SPM (polarized vertically) closes the robot. However, when the polarization direction of SPM is adjusted to be horizontal, the resulting milli-FRs will be recombined to scale up to centi-FR, as illustrated by the schematic diagram at the bottom. (**D**) Image sequences show the experimental splitting (scale down to micro-FR) and recombination (scale up to milli-FR) process of the milli-FR when increasing or decreasing the frequency of the rotating magnetic field. The schematic diagrams in the lower right corner illustrate the state of SPM during the process in a side view, where the arrow pointing upward represents an increase in the SPM's rotation frequency, otherwise representing a decrease. (**E**) Image sequences show large-scope controlled fluid induced by chain-like micro-FR assemblies. The blue and red boxes mark the positions of some tracer particles, which are acted by ferrofluid fragments floating on the liquid surface, and the white arrows show the adjusting process of the controlled fluid at reference positions. (**F**) Emergency and control of the resulting micro-FRs swarm with different patterns: vortex swarm and matrix swarm.

milli-FRs get away from each other because of the induced magnetic repulsion. Last, a magnetic sphere (diameter, 1.5 mm) with an extremely local magnetic field B_{local} is manually transferred to the bottom of a candidate milli-FR to lock it, since the B_{local} can only produce an effective driving force in a limited range (≈2 mm), enabling an individual manipulation method of the locked milli-FRs without disturbing its neighbors, as demonstrated by fig. S11B and movie S6. In this way, we can subtly separate milli-FRs from the dense area one by one without necessarily relying on the surrounding environment.

However, one cannot continually split the milli-FR using the above method because a smaller volume of milli-FR results in weak repulsive forces among presegmentations that fail to overcome surface tension and the enrichment effect of magnetic gradient forces (see fig. S12 and note S3 for more details). The minimum diameter of the resulting milli-FRs appears when d_h is within 5 to 8 mm, where the minimum diameter of milli-FRs is around 1.8 mm. Here, as shown in Fig. 5B, to realize the further splitting of the milli-FR, we proposed an intelligent strategy based on the M^{3}RA system by tuning the rotation speed of the $\boldsymbol{B}_a$. A close inspection of Fig. 5D and movie S5 indicates that when the milli-FR rotates quickly enough under the strong rotating magnetic field produced by the SPM underneath, it is capable of splitting into multiple micro-FRs. This result may be explained by the fact that the milli-FR is stretched to an ellipsoid-like shape by the actuation magnetic field during the experimental process, making the shear forces suffered by the milli-FR anisotropic, that is, the closer to the end, the greater the shear forces are. Therefore, when the rotation speed is fast enough, the milli-FR is forced to break up from the ends, and with an increase in rotation speed, the SMFR can be split many times. This can be demonstrated in Fig. 5D, which shows that a milli-FR is separated into 14 micro-FRs one by one by gradually increasing the rotation frequency (from 1 to 120 Hz). Even more interesting, these resulting

micro-FR formations are aligned along a straight line as a chain-like assembly because of the time-averaged attraction $U(r)_{attr} = -\mu_0 m^2/8\pi r^3$, where r is the dipole's center-to-center distance, μ_0 is the permeability of vacuum, and m is the dipole strength. In addition, this process has proven excellent reversibility; that is, micro-FRs can recombine into milli-FR by reducing the rotation frequency (from 120 to 1 Hz), as shown in the latter part of Fig. 5D. Therefore, by simply turning the actuation frequency, it is possible to achieve the on-demand scale reconfiguration of SMFRs. As shown in Fig. 5E and movie S5, the unique chain-like structure enables the assembled micro-FRs to produce a large scope of controllable flows in their arrangement direction. The tracer particles (ferrofluid fragments) on the liquid surface reflect the controllability and effect range of the resulting fluid. To theoretically analyze the strengthening effect of the chain-like assembly on the secondary fluid, we simulated the velocity of the resulting flow while considering the presence of a stationary plane boundary (see "Numerical simulation of fluid" section). As indicated in fig. S13 and movie S5, the fluid directly above the assembly is accelerated multiple times as it passes each micro-FR, until it reaches a huge jet velocity before leaving, and then drives a large scope of fluid motion, which potentially has great research significance for realizing efficient stirring and noncontact manipulation in a low Reynolds number environment.

Notwithstanding, it is challenging to achieve independent control of the resulting micro-FRs after splitting a milliscale one, since they are so close to each other that they can be regarded as exposed to the identical actuation field; therefore, they have synchronized and consistent behavior. Instead of actuating them individually, as shown in Fig. 5F, we proposed a more practical strategy based on the idea of swarm control, which is recognized as a more optimal, robust, and efficient driving mode for miniature robots (*36*). Figure S14 and movie S6 show the swarm control principle and experimental results of micro-FRs, where a single milli-FR is split into a series of micro-FRs and then controlled to locomote while maintaining a matrix pattern under the action of the M^{3}RA. The micro-FR swarm can be switched between the matrix pattern and vortex pattern by adjusting the SPM's rotating axis (z axis or any axis on the horizontal plane). As proved by previous works (*48*, *49*), realizing swarm control not only can retain the flexible characteristics of the small-scale robots due to their small size but also greatly improves their control efficiency and movement speed, which enables them to cross complex environments, such as a narrow channel and an undulating surface more efficiently.

Combined locomotion, deformation, and scale reconfiguration of the SMFR in sharply variable spaces

As shown in Fig. 6A, the cross-sectional dimensions of channels in many organs or tissues inside the human body may change markedly. Therefore, to realize the application in vivo, the miniature robot must deal with this situation. Targeted drug delivery, for example, requires miniature robots capable of accessing sophisticated structured environments with varying characteristic scales, such as blood vessels and natural orifices. To tackle this challenge, as a proof-of-concept demonstration, we achieved trans-scale control of the SMFR in a specially designed phantom to mimic their motion behaviors when navigating scale-varying biology environments by tuning the magnetic field according to the local environmental conditions to achieve combined locomotion, deformation, and scale reconfiguration in situ (Fig. 6B).

Figure 6C and movie S7 show that the experimental scene started from a centimeter-scale square maze with width-varying channels. After the maze was a millimeter-scale meandering channel that gradually extended to a micrometer-scale circular maze. To navigate the SMFR through the phantom, we applied different control signals through the M^{3}RA system. First, the SMFR was guided to cross the first half of the square maze by a standing SPM under the translation of the x-y motorized stage. When encountering a narrow gap, the centi-FR was stretched along the channel by rotating the SPM horizontally to squeeze through the narrow part. However, when the width of the walkable path changed significantly, the centi-FR no longer crossed through slight deformation. Instead, in this case, we enhanced the magnetic field and vertical magnetic field gradient around the centi-FR by decreasing the d_h to split the centi-FR into multiple milli-FRs. Next, the SPM was moved away to smartly control redundant milli-FRs to leave the region of interest (ROI) with only one left behind. After that, the SPM was quickly transported horizontally to get close to the ROI again alone. Then, the selected milli-FR was controlled to pass through the winding millimeter-scale narrow channel through simultaneous rotation and translation. Last, as the locally enlarged drawing of the red box labeled part (Fig. 6D) shows, before entering the microscale circular maze, the milli-FR was ulteriorly split into micro-FRs by increasing the rotation speed (up to 50 Hz), which enabled them to shuttle the circular maze freely and finally merge in the central region. Note that these complex manipulations of miniature robots are not possible using previous approaches because of the extremely marked changes in the environmental scale in this kind of application scenario.

DISCUSSION

Magnetically actuated miniature soft robots could potentially enable direct access to currently difficult-to-reach regions inside the human body for minimally invasive medical operations. However, research has mainly focused on robots with immutable scales, with their active locomotion accessible only when the cross-sectional dimension of these confined spaces is comparable to that of the robot. Therefore, their functionalities are currently restricted by their predesigned scales. Moreover, it is still challenging to achieve free control of miniature robots with multiple scales simultaneously, restricted by the lack of compatibility control methods, which prevents us from entirely using the volume advantages of miniature robots with varying scales in critical engineering and biomedical applications. Here, we realized the SMFRs by programming external magnetic fields spatiotemporally. We also propose a series of adaptive control strategies for reconfiguring SMFRs' scale and deformation to achieve trans-scale motion control by designing a M^{3}RA system through hybridizing permanent and electric magnets, which allows the SMFR to achieve free navigation in confined spaces with a notable scale change. In addition, functional maneuvers were carefully presented to prove the effectiveness of our method and illustrate the potential utility of the SMFRs' advanced dexterity. Investigating the reconfiguration and trans-scale control of SMFRs improved our understanding of their dynamic organization and motion behaviors on various scales. Thus, the presented combination of locomotion, deformation, and scale reconfiguration of the SMFRs markedly enhanced the functionality and practicability of the miniature robot for potential applications in the biomedical

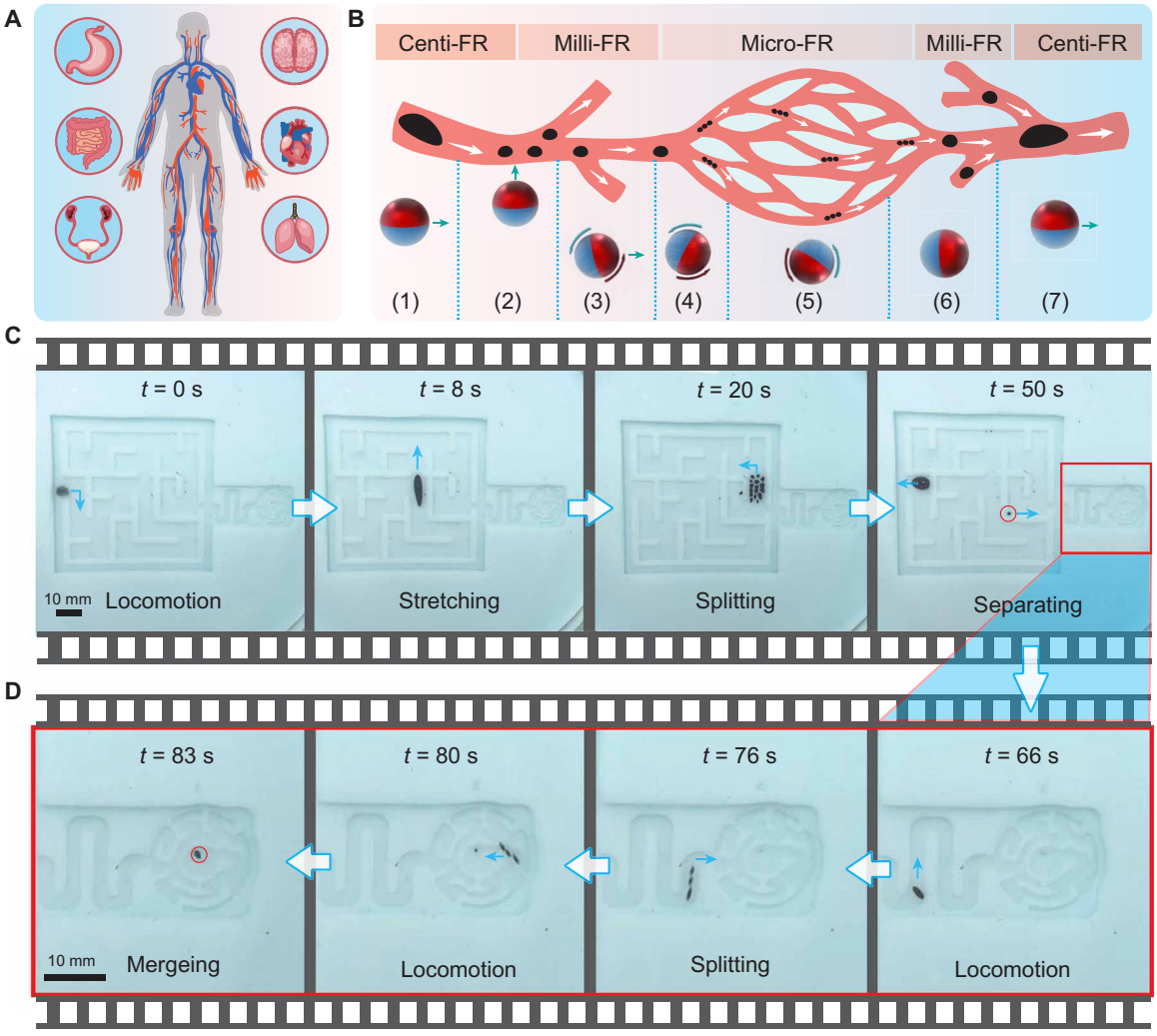

Fig. 6. Locomotion of the SMFR in a dimension-varying structure based on the combined locomotion, deformation, and scale reconfiguration. (**A**). Organs and tissues with multiscale structures in the human body. (**B**) Schematics of an SMFR crossing blood vessel–like structures with scale-varying gaps: (i) locomotion of the centi-FR; (ii) scaling down to milli-FR; (iii) locomotion of milli-FR; (iv) scaling down to micro-FR; (v) locomotion of micro-FR; (vi) scaling up to milli-FR; (vii) scaling up to centi-FR and recycling. (**C**) Sequential video snapshots demonstrating the combined locomotion, deformation, and scale reconfiguration of a centi-FR by squeezing through a maze with specially designed narrow features. (**D**) The local enlarged drawing of the red box labeled part in (C). From the experimental results, one can see the process of an SMFR crossing a structured environment with scale-varying features through scale reconfiguration.

and microassembly fields. For example, when in a relatively wide work space, one can improve the SMFR's task execution capabilities and efficiency by making them larger through the scale-up strategy; however, when encountering extremely narrow and restricted environments, one can scale them down into a swarm by the splitting strategy, making them very suitable for navigating tubular or slit-like lumen structures with sharply variable cross-sectional dimensions inside the human body.

In general, as we have demonstrated, since the SMFR's design is not fixed, changing the magnetic field control inputs can enable different locomotion modes, deformation, and even the scale of the robot, which are expected to make substantial progress and gradually realize their applications in practical scenes. Realizing the trans-scale motion control of SMFRs makes it possible to take full use of their scale-induced advantages through adaptively matching the constrained environments. Achieving these dexterous functions of miniature robots is the primary motivation behind this study. However, even though the experiments conducted in this study are two-dimensional (2D), it is possible to steer the robot in 3D confined spaces by generating rotating magnetic fields and magnetic gradients in arbitrary planes in 3D space. Therefore, additional efforts need to be made to realize the motion and shape control of the SMFR in 3D spaces, since many application scenarios must be implemented in such environments (*3*, *6*, *18*). Moreover, this work mainly focused on the motion control and scale reconfiguration of SMFRs without considering their biomedical functionality. Therefore, achieving some application-oriented tasks, such as SMFR-based targeted cargo delivery (*22*), precise local magnetic hyperthermia (*50*), or selective occlusion of tumor blood vessels (*51*), would also be of great interest and thus another potential direction for future research.

MATERIALS AND METHODS

Modeling of the magnetic field and forces

Magnetic force and torque

Magnetic actuation was conducted by imparting magnetic force and/or torque to the SMFR through remotely applied magnetic fields. In newton meters, the torque on a targeted SMFR with a magnetic moment $\boldsymbol{m}$ in magnetic field $\boldsymbol{B}$ is expressed as follows (*52*)

$$\tau_m = \boldsymbol{m} \times \boldsymbol{B} = \begin{bmatrix} 0 & \boldsymbol{B}_z & -\boldsymbol{B}_y \\ -\boldsymbol{B}_z & 0 & \boldsymbol{B}_x \\ \boldsymbol{B}_y & -\boldsymbol{B}_x & 0 \end{bmatrix} \begin{bmatrix} \boldsymbol{m}_x \\ \boldsymbol{m}_y \\ \boldsymbol{m}_z \end{bmatrix} \quad (2)$$

This equation indicates that the torque tends to align the magnetic moment $\boldsymbol{m}$ with the applied field $\boldsymbol{B}$. Meanwhile, the force on the magnetic moment in newtons is expressed as follows

$$\boldsymbol{F}_m = (\boldsymbol{m} \cdot \nabla)\boldsymbol{B} \quad (3)$$

where ∇ is a gradient operator. Since there is no electric current flowing through the region occupied by the body, the quasi-static magnetic field can be described by Maxwell's equation as $\nabla \times \boldsymbol{B} = 0$ and $\nabla \cdot \boldsymbol{B} = 0$ (*52*, *53*). This enables Eq. 2, after some manipulation, to be expressed in a more straightforward form

$$\boldsymbol{F}_m = \begin{bmatrix} \frac{\partial \boldsymbol{B}_x}{\partial x} & \frac{\partial \boldsymbol{B}_x}{\partial y} & \frac{\partial \boldsymbol{B}_x}{\partial z} \\ \frac{\partial \boldsymbol{B}_x}{\partial y} & \frac{\partial \boldsymbol{B}_y}{\partial y} & \frac{\partial \boldsymbol{B}_y}{\partial z} \\ \frac{\partial \boldsymbol{B}_x}{\partial z} & \frac{\partial \boldsymbol{B}_F}{\partial z} & -\left(\frac{\partial \boldsymbol{B}_x}{\partial x} + \frac{\partial \boldsymbol{B}_y}{\partial y}\right) \end{bmatrix} \begin{bmatrix} \boldsymbol{m}_x \\ \boldsymbol{m}_y \\ \boldsymbol{m}_z \end{bmatrix} \quad (4)$$

Modeling of the magnetic dipole

The dipole model is widely used to model the magnetic field of permanent magnets or electric coils with soft magnetic cores because it provides an analytical expression convenient for calculation. The magnetic flux density $\boldsymbol{B}$ produced by a dipole (fig. S15A) at the ROI is equal to (*54*)

$$\boldsymbol{B}(\boldsymbol{m};\boldsymbol{r}) = \frac{\mu_0}{4\pi}\left(\frac{3\boldsymbol{m} \cdot \boldsymbol{r}}{r^5}\boldsymbol{r} - \frac{\boldsymbol{m}}{r^3}\right) \quad (5)$$

where $\mu_0 = 4\pi \times 10^{-7}$ is the air permeability, $\boldsymbol{r}$ is the vector pointing from the magnet center to the targeted point $P(r, \theta)$, and $\boldsymbol{m}$ is the magnetic moment of the dipole source in units Am^2, which can be found by integrating the magnetization $\boldsymbol{M}$ over the volume as $\boldsymbol{m} = \int \boldsymbol{M}dV$. For systems with multiple permanent magnets, the total magnetic filed obeys the superposition law.

Modeling of the coil with the air core

In the analytical calculation, each turn of the solenoid coil was assumed to be of a single circular loop. The magnetic flux density $\boldsymbol{B}$ at any point due to a single current loop of radius a, as shown in fig. S15B, can be computed by evaluating the curl of the magnetic vector potential $\boldsymbol{A}$. With the current loop located in and symmetric to the x-y plane, $\boldsymbol{A}$ is given by (*55*)

$$\boldsymbol{A}_\varphi(r,\theta) = \frac{\mu_0 aI}{4\pi}\int_0^{2\pi} \frac{\cos\varphi d\varphi}{\sqrt{a^2 + r^2 - 2ar\sin\theta\cos\varphi}} \quad (6)$$

where r, θ, and φ are spherical coordinates, I is the loop current, and μ_0 is the permeability of free space. The curl of Eq. 6 can be simplified in Cartesian coordinates as follows

$$\begin{aligned} \boldsymbol{B}_x &= \frac{Cxz}{2\alpha^2\beta\rho^2}((a^2 + r^2)E(k^2) - \alpha^2 K(k^2)) \\ \boldsymbol{B}_y &= \frac{Cyz}{2\alpha^2\beta\rho^2}((a^2 + r^2)E(k^2) - \alpha^2 K(k^2)) \\ \boldsymbol{B}_z &= \frac{C}{2\alpha^2\beta}((a^2 - r^2)E(k^2) + \alpha^2 K(k^2)) \end{aligned} \quad (7)$$

where $\rho^2 \equiv x^2 + y^2$, $r^2 \equiv \rho^2 + z^2$, $\alpha^2 \equiv a^2 + r^2 - 2a\rho$, $\beta^2 \equiv a^2 + R^2 + 2a\rho$, $k^2 \equiv 1 - \alpha^2/\beta^2$, and $C \equiv \mu_0 I/\pi$. Here, $K(k^2)$ and $E(k^2)$ are the complete elliptical integrals of the first and second kinds, respectively. After calculating the magnetic field due to a single loop, these fields are integrated for the whole coil in all axial directions.

Numerical simulation of fluid

The velocity of the flow $\boldsymbol{u}$ generated by a micro-FR with a radius of a at an angular velocity of Ω, and a distance h from the stationary plane boundary can be evaluated by the tensorial equation, as developed in the study of Blake and Chwang (*56*)

$$u = a^3\left[\frac{\epsilon_{ijk}\Omega_j\hat{r}_k}{|\hat{r}|^3} - \frac{\gamma_{ijk}\Omega_j R_k}{|R|^3} + 2h\epsilon_{kjz}\Omega_j\left(\frac{\delta_{ik}}{|R|^3} - \frac{3R_iR_k}{|R|^5}\right) + 6\epsilon_{kjz}\frac{\Omega_j R_i R_k R_z}{|R|^5}\right] \quad (8)$$

where u is the velocity vector, $\hat{r} = \sqrt{(x-x_1)^2 + (y-y_1)^2 + (z-z_1)^2}$ is the position from the center of the micro-FR, $R = \sqrt{(x-x_1)^2 + (y-y_1)^2 + (z+z_1)^2}$ is the position of its image, (x_1, y_1, z_1), (x, y, z) are the locations of the micro-FR and target position for the fluid velocity calculation, respectively, and ϵ is the Levi-Civita tensor. When $Re \ll 1$, Stokes equations reduces to a linear equation, which makes the principle of superposition available; therefore, the induced fluid field by a chain-like micro-FR assembly is the sum of the fluid fields generated by an array of N micro-FRs as $\boldsymbol{u} = \sum_{i=1}^{N} \boldsymbol{u}_i$.

Experimental setup and systems

Figure S16 illustrates the framework of the physical composition of the M^{3}RA system. The computer as the host of the M^{3}RA system was used to display the interactive interface and perform data visualization; a DAQ board (NI-6259, National Instruments) was used to output and transmit the desired control signals in an addressable manner. Four homemade power amplifiers were used to amplify the signals before connecting with the coils, and they are capable of a 75-V peak voltage and an 8-A load current. The broad view field above the device allowed the installation of an upright microscope to obtain the position and potential orientation information of the SMFR, with the resolution of the installed charge-coupled device (CCD) camera being 1600 × 1200.The control module, possessing an Intel Core i7 3.0-GHz processor, was used to run the LabVIEW-based customized software that includes real-time imaging tracking programs and control algorithms, which enables the M^{3}RA system to output preprogrammed control signals or receive remote control signals from a joystick to guarantee the dexterity of the M^{3}RA system. Moreover, to ensure the M^{3}RA system has a reasonable structure and suitable workspace for potential clinical examinations, a three-axis motorized translation stage (25-cm rang, 0.2-mm precision

on *x*-*y* axes; 10-cm rang, 0.1-mm precision on *z* axe) was introduced to ensure that the M^{3}RA system is always located near the ROI (fig. S2C).

Programming methods of the spatiotemporal actuation magnetic field

To generate the powerful omnidirectional actuation magnetic field $\boldsymbol{B}_m$, the arranged electromagnets are programmed to guarantee the desired post of the SPM by generating $\boldsymbol{B}_b$, to which the SPM will naturally align, rather than explicitly controlling the torque. Assuming that the magnetic field vector generated by coil$_i$ with a unit current at target point $\boldsymbol{P}$ is $\widetilde{\boldsymbol{B}}_i = (\widetilde{\boldsymbol{B}}^x{}_i, \widetilde{\boldsymbol{B}}^y{}_i, \widetilde{\boldsymbol{B}}^z{}_i)$. Regarding a combination of several coils, the contribution matrix $\beta(\boldsymbol{P})$ can be composed of multiple $\widetilde{\boldsymbol{B}}$ derived from every coil. Moreover, the net magnetic flux density can be calculated using the linear superposition of each coil's magnetic flux density contribution. Therefore, at any given point in the workspace, the magnetic field due to actuating several given electromagnets with internal current $i = [i_1 \cdots i_n]$ can be expressed as

$$\boldsymbol{B}(\boldsymbol{P}) = \beta(\boldsymbol{P}) \begin{bmatrix} i_1 \\ \vdots \\ i_n \end{bmatrix} \tag{9}$$

where $\beta(\boldsymbol{P}) = [\widetilde{\boldsymbol{B}}_1(\boldsymbol{P}) \cdots \widetilde{\boldsymbol{B}}_n(\boldsymbol{P})]$, and n is the number of coils. The electrical current in each coil to generate the required magnetic field can be determined considering the linear relation of magnetic field and electrical current, as long as the inverse or pseudo-inverse of the contribution matrix $\beta(\boldsymbol{P})$ can be found. Therefore, the required current $[i_0 \ldots i_3]$ to achieve the desired magnetic field can be calculated as

$$\begin{bmatrix} i_0 \\ i_1 \\ i_2 \\ i_3 \end{bmatrix} = \boldsymbol{\beta}(\boldsymbol{P})^{\dagger} \begin{bmatrix} B_x \\ B_y \\ B_z \end{bmatrix} \tag{10}$$

where † represents the pseudo-inverse of this application. To find the contribution matrix caused by all coils, we assume that the SPM is always located at the intersection of their axes. As demonstrated in fig. S2, axial directions of all coils coincide with the diagonal of the cubic space formed by the center points of the four coils, which guarantees that the flux density generated by each coil at the origin is equal in the *x*, *y*, and *z* axial, with a same scale factor α. Last, the $\boldsymbol{\beta}$ can be simply written as

$$\boldsymbol{\beta}(\boldsymbol{P}) = \alpha \begin{bmatrix} 1 & -1 & -1 & 1 \\ 1 & 1 & -1 & -1 \\ -1 & -1 & -1 & -1 \end{bmatrix} \tag{11}$$

Motion control scheme of the SMFR

Here, to control the position of the SMFR on a predetermined trajectory in addition to an open-loop control method based on the joystick, we also proposed a closed-loop control method to make the SMFR more controllable. To achieve this aim, the desired paths were segmented into a series of steps, including a point-to-point breakdown of the desired path, and fed to the controller in the form of an array. The directions of the actuation magnetic field were controlled by a closed-loop controller to steer the SMFR toward the next point in the array. As the SMFR approached the desired position, the controller moved to the next point in the path, methodically moving through each predefined position path.

As the control architecture shows in fig. S8, an observer of the robot's position was established using the LabVIEW-in-built Mean-Shift algorithm and Kalman filter algorithm to enhance accuracy and noise immunity. Moreover, the closed-loop controller used in this research was written in LabVIEW, which changes the steering angle θ and frequency of the input magnetic field based on measuring the distance between the current location (x_c and y_c) and reference location (x_r and y_r)

$$\begin{aligned} v_s &= k \min\left(\sqrt{e_x^2 + e_y^2} + f_{\min}, f_{\text{stepout}}\right) \\ \Delta\theta &= \arctan\left(\frac{e_x}{e_y}\right) \end{aligned} \tag{12}$$

where k is the ratio of the rotating speed to the translation velocity of the SMFR, which can be measured through experiments. $e_x = x_c - x_r$, $e_y = y_c - y_r$, $f_{\max}$ is the upper limit of the driving frequency, and $f_{\min}$ is the minimum driving frequency capable of overcoming friction, Brownian motion, or other external disturbances.

Magnetic field measurements

The magnetic field was measured using a Hall sensor (TLE493D-W2B6, Infineon Technologies Inc.), which can detect the strength of a magnetic field in all three dimensions, i.e., the *x*, *y*, and *z* axes. The output signal from the Hall sensor was acquired through the serial port. The three components of the magnetic field (B_x, B_y, and B_z) generated by the SPM or coils were measured with the module attached to the three-axis motorized translation stage, which was also used to perform all the ferrofluidic robot actuation experiments and a *z* translation stage. LabVIEW-based upper computer software was developed to realize the traversal of the sensor to any point within the workplace.

Fabrication of the hydrogel maze

As shown in fig. S17, the polypodium acrylate hydrogel maze was synthesized using the free radical polymerization method. In a typical experiment, sodium acrylate (400 mg), *N*,*N*′-methylenebis-acrylamide, dye (10 μl), and $K_2S_2O_8$ (15 mg) were dissolved in deionized water and ultrasonicated for 30 min. Then, $C_6H_{16}N_4$ (10 μl) was added into the solution after a female maze mold that was 3D printed from polylactic acid was immersed. After 10 hours of polymerization at room temperature, a hydrogel maze with various special structures was finally obtained. Last, the maze was removed for later use.

Preparation of the SMFR

Ferrofluids with a density of 1.43 g cm^{-3} dynamic viscosities of 8 mPa · s (EMG 901; Ferrotec Corporation) were used in the experiments. The properties of the ferrofluids are summarized in table S2. Figure 2A shows the transmission electron microscope image of the iron oxide nanoparticles in ferrofluids. The pipette gun was used to prepare centi-FR of a specific size. The milli-FR and micro-FR were prepared by the splitting effect of an external magnetic field, as described in the main manuscript.

SUPPLEMENTARY MATERIALS

Supplementary material for this article is available at https://science.org/doi/10.1126/sciadv.abq1677

REFERENCES AND NOTES

1. F. Soto, J. Wang, R. Ahmed, U. Demirci, Medical micro/nanorobots in precision medicine. *Adv. Sci.* **7**, 2002203 (2020).
2. B. J. Nelson, I. K. Kaliakatsos, J. J. Abbott, Microrobots for minimally invasive medicine. *Annu. Rev. Biomed. Eng.* **12**, 55–85 (2010).
3. J. Li, B. E. F. de Avila, W. Gao, L. Zhang, J. Wang, Micro/nanorobots for biomedicine: Delivery, surgery, sensing, and detoxification. *Sci. Robot.* **2**, eaam6431 (2017).
4. M. Sitti, *Mobile Microrobotics* (MIT Press, 2017).
5. K. E. Peyer, L. Zhang, B. J. Nelson, Bio-inspired magnetic swimming microrobots for biomedical applications. *Nanoscale* **5**, 1259–1272 (2013).
6. M. Sitti, Miniature soft robots-Road to the clinic. *Nat. Rev. Mater.* **3**, 74–75 (2018).
7. J. J. Abbott, K. E. Peyer, M. C. Lagomarsino, L. Zhang, L. Dong, I. K. Kaliakatsos, B. J. Nelson, How should microrobots swim? *Int. J. Robot. Res.* **28**, 1434–1447 (2009).
8. Z. Ren, W. Hu, X. Dong, M. Sitti, Multi-functional soft-bodied jellyfish-like swimming. *Nat. Commun.* **10**, 2703 (2019).
9. R. Mhanna, F. Qiu, L. Zhang, Y. Ding, K. Sugihara, M. Zenobi-Wong, B. J. Nelson, Artificial bacterial flagella for remote-controlled targeted single-cell drug delivery. *Small* **10**, 1953–1957 (2014).
10. F. Qiu, S. Fujita, R. Mhanna, B. R. Simona, B. J. Nelson, Magnetic helical microswimmers functionalized with lipoplexes for targeted gene delivery. *Adv. Funct. Mater.* **25**, 1666–1671 (2015).
11. H. Zhang, Z. Li, C. Gao, X. Fan, Y. Pang, T. Li, Z. Wu, H. Xie, Q. He, Dual-response biohybrid neutrobots for active target delivery. *Sci. Robot.* **6**, eaaz9519 (2021).
12. Z. Wu, J. Troll, H. H. Jeong, Q. Wei, M. Stang, F. Ziemssen, Z. Wang, M. Dong, S. Schnichels, T. Qiu, P. Fischer, A swarm of slippery micropropellers penetrates the vitreous body of the eye. *Sci. Adv.* **4**, eaat4388 (2018).
13. J. Čejková, T. Banno, M. M. Hanczyc, F. Štěpánek, Droplets as liquid robots. *Artif. Life* **23**, 528–549 (2017).
14. F. Li, J. Shu, L. Zhang, N. Yang, J. Xie, X. Li, L. Cheng, S. Kuang, S. Tang, S. Zhang, W. Li, L. Sun, D. Sun, Liquid metal droplet robot. *Appl. Mater. Today* **19**, 100597 (2020).
15. N. J. Cira, A. Benusiglio, M. Prakash, Vapour-mediated sensing and motility in two-component droplets. *Nature* **519**, 446–450 (2015).
16. X. Fan, M. Sun, L. Sun, H. Xie, Ferrofluid droplets as liquid microrobots with multiple deformabilities. *Adv. Funct. Mater.* **30**, 2000138 (2020).
17. M. Latikka, M. Backholm, A. Baidya, A. Ballesio, A. Serve, G. Beaune, J. V. Timonen, T. Pradeep, R. H. Ras, Ferrofluid microdroplet splitting for population based microfluidics and interfacial tensiometry. *Adv. Sci.* **7**, 2000359 (2020).
18. R. Ahmed, M. Ilami, J. Bant, B. Beigzadeh, H. Marvi, A shapeshifting ferrofluidic robot. *Soft Robot.* **8**, 687–698 (2021).
19. A. Nacev, A. Komaee, A. Sarwar, R. Probst, S. H. Kim, M. Emmert-Buck, B. Shapiro, Towards control of magnetic fluids in patients: Directing therapeutic nanoparticles to disease locations. *IEEE Control Syst. Mag.* **32**, 32–74 (2012).
20. A. Komaee, B. Shapiro, Magnetic steering of a distributed ferrofluid spot towards a deep target with minimal spreading. *Proc. IEEE Conf. Decision Control* , 7950–7955 (2011).
21. M. Zhou, Z. Wu, Y. Zhao, Q. Yang, W. Ling, Y. Li, H. Xu, C. Wang, X. Huang, Droplets as carriers for flexible electronic Devices. *Adv. Sci.* **6**, 1901862 (2019).
22. J. S. Sander, R. M. Erb, C. Denier, A. R. Studart, Magnetic transport, mixing and release of cargo with tailored nanoliter droplets. *Adv. Mater.* **24**, 2582–2587 (2012).
23. F. Serwane, A. Mongera, P. Rowghanian, D. A. Kealhofer, A. A. Lucio, Z. M. Hockenbery, O. Campàs, In vivo quantification of spatially varying mechanical properties in developing tissues. *Nat. Methods* **14**, 181–186 (2017).
24. W. Yu, H. Lin, Y. Wang, X. He, N. Chen, K. Sun, D. Lo, B. Cheng, C. Yeung, J. Tan, D. D. Carlo, S. Emaminejad, A ferrobotic system for automated microfluidic logistics. *Sci. Robot.* **5**, eaba4411 (2020).
25. J. V. I. Timonen, M. Latikka, L. Leibler, R. H. A. Ras, O. Ikkala, Switchable static and dynamic self-assembly of magnetic droplets on super-hydrophobic surfaces. *Science* **341**, 253–257 (2013).
26. D. Son, M. C. Ugurlu, M. Sitti, Permanent magnet array-driven navigation of wireless millirobots inside soft tissues. *Sci. Adv.* **7**, eabi8932 (2021).
27. W. Lee, S. Jeon, J. Nam, G. Jang, Dual-body magnetic helical robot for drilling and cargo delivery in human blood vessels. *J. Appl. Phys.* **117**, 17B314 (2015).
28. C. K. Schmidt, M. M. Sánchez, R. J. Edmondson, O. G. Schmidt, Engineering microrobots for targeted cancer therapies from a medical perspective. *Nat. Commun.* **11**, 5618 (2020).
29. W. Hu, G. Z. Lum, M. Mastrangeli, M. Sitti, Small-scale soft-bodied robot with multimodal locomotion. *Nature* **554**, 81–85 (2018).
30. Y. Zhang, K. Yan, F. Ji, L. Zhang, Enhanced removal of toxic heavy metals using swarming biohybrid adsorbents. *Adv. Funct. Mater.* **28**, 1806340 (2018).
31. A. P. Francesch, J. Giltinan, M. Sitti, Multifunctional and biodegradable self-propelled protein motors. *Nat. Commun.* **10**, 1–10 (2019).
32. D. Jang, J. Jeong, H. Song, S. K. Chung, Targeted drug delivery technology using untethered microrobots: A review. *J. Micromech. Microeng.* **29**, 053002 (2019).
33. M. Luo, Y. Feng, T. Wang, J. Guan, Micro−/nanorobots at work in active drug delivery. *Adv. Funct. Mater.* **28**, 1706100 (2018).
34. A. Ramos-Sebastian, S. J. Gwak, S. H. Kim, Multimodal locomotion and active targeted thermal control of magnetic agents for biomedical applications. *Adv. Sci.* **9**, 2103863 (2022).
35. H. Ceylan, I. C. Yasa, U. Kilic, W. Hu, M. Sitti, Translational prospects of untethered medical microrobots. *Prog. Biomed. Eng.* **1**, 012002 (2019).
36. J. Yu, D. Jin, K. F. Chan, Q. Wang, K. Yuan, L. Zhang, Active generation and magnetic actuation of microrobotic swarms in bio-fluids. *Nat. Commun.* **10**, 1–12 (2019).
37. M. Latikka, M. Backholm, J. V. I. Timonen, R. H. A. Ras, Wetting of ferrofluids: Phenomena and control. *Curr. Opin. Colloid Interface Sci.* **36**, 118–129 (2018).
38. L. Huang, T. Hädrich, On the accurate large-scale simulation of ferrofluids. *ACM. T. Graphic* **38**, 1–15 (2019).
39. J. D. Vicente, D. J. Klingenberg, R. H. Alvarez, Magnetorheological fluids: A review. *Soft Matter* **7**, 3701–3710 (2011).
40. M. Qiu, S. Afkhami, C. Chen, J. J. Feng, Interaction of a pair of ferrofluid drops in a rotating magnetic field. *J. Fluid Mech.* **846**, 121–142 (2018).
41. M. I. Shliomis, How a rotating magnetic field causes ferrofluid to rotate. *Phy. Rev. Fluids* **6**, 043701 (2021).
42. Z. Yang, L. Zhang, Magnetic actuation systems for miniature robots: A review. *Adv. Intell. Syst.* **2**, 2000082 (2020).
43. X. Fan, X. Dong, A. C. Karacakol, H. Xie, M. Sitti, Reconfigurable multifunctional ferrofluid droplet robots. *Proc. Natl. Acad. Sci. U.S.A.* **117**, 27916–27926 (2020).
44. C. Chen, H. Hsueh, S. Wang, Y. Li, Self-assembly and novel planetary motion of ferrofluid drops in a rotational magnetic field. *Microfluid. Nanofluid.* **18**, 795–806 (2015).
45. P. Rowghanian, C. D. Meinhart, O. Campás, Dynamics of ferrofluid drop deformations under spatially uniform magnetic fields. *J. Fluid Mech.* **802**, 245–262 (2016).
46. T. Jamin, Y. Djama, J. C. Bacri, E. Falcon, Tuning the resonant frequencies of a drop by a magnetic field. *Phys. Rev. Fluids* **1**, 021901 (2016).
47. X. Dong, M. Sitti, Controlling two-dimensional collective formation and cooperative behavior of magnetic microrobot swarms. *Int. J. Robot. Res.* **39**, 617–638 (2020).
48. H. Xie, M. Sun, X. Fan, Z. Lin, W. Chen, L. Wang, L. Dong, Q. He, Reconfigurable magnetic microrobot swarm: Multimode transformation, locomotion, and manipulation. *Sci. Robot.* **4**, eaav8006 (2019).
49. G. Gardi, S. Ceron, W. Wang, K. Petersen, M. Sitti, Microrobot collectives with reconfigurable morphologies, behaviors, and functions. *Nat. Commun.* **13**, 1–14 (2022).
50. I. Sharifi, H. Shokrollahi, S. Amiri, Ferrite-based magnetic nanofluids used in hyperthermia applications. *J. Magn. Magn. Mater.* **324**, 903–915 (2012).
51. M. Fabbrini, E. Trachsel, P. Soldani, S. Bindi, P. Alessi, L. Bracci, H. Kosmehl, L. Zardi, D. Neri, P. Neri, Selective occlusion of tumor blood vessels by targeted delivery of an antibody-photosensitizer conjugate. *Int. J. Cancer* **118**, 1805–1813 (2006).
52. J. J. Abbott, E. Diller, A. J. Petruska, Magnetic methods in robotics. *Annu. Rev. Control Robot. Autom. Syst.* **3**, 57–90 (2020).
53. S. Jeon, A. K. Hoshiar, K. Kim, S. Lee, E. Kim, S. Lee, J. Kim, B. J. Nelson, H. J. Cha, B. J. Yi, H. Choi, A magnetically controlled soft microrobot steering a guidewire in a three-dimensional phantom vascular network. *Soft Robot.* **6**, 54–68 (2019).
54. M. P. Kummer, J. J. Abbott, B. E. Kratochvil, R. Borer, A. Sengul, B. J. Nelson, OctoMag: An electromagnetic system for 5-DOF wireless micromanipulation. *IEEE T. Robot.* **26**, 1006–1017 (2010).
55. A. Caciagli, R. J. Baars, A. P. Philipse, B. W. M. Kuipers, Exact expression for the magnetic field of a finite cylinder with arbitrary uniform magnetization. *J. Magn. Magn. Mater.* **456**, 423–432 (2018).
56. J. R. Blake, A. T. Chwang, Fundamental singularities of viscous flow. *J. Eng. Math.* **8**, 23–29 (1974).

Acknowledgments

Funding: This work was partially supported by the Natural Science Foundation of Jiangsu province (grant no. BK20210717), National Natural Science Foundation of China (grant no. 62103294 and 61925304), China Postdoctoral Science Foundation (grant nos. 7111795721 and 7111785821), and Postdoctoral Research Support of Jiangsu province (grant no. 7111751621). M.S. was funded by the Max Planck Society and the European Research Council (ERC) Advanced Grant SoMMoR project with grant no. 834531 and German Research Foundation

(DFG) Soft Material Robotic Systems (SPP 2100) Program with grant no. 2197/3-1. The authors also would like to acknowledge the support from Robot and Microsystem Research Center of Soochow University. **Author contributions:** M.S., Z.Y., and X.F. conceived and designed the research. X.F., Y.J., and M.L. analyzed the experimental and calculated data. Y.Z. and C.T. prepared the ferrofluid droplets. L.M. wrote the simulation and image processing programs. L.S. and H.X. directed the project. All authors wrote the manuscript. **Competing interests:** The authors declare that they have no competing interests. **Data and materials availability:** All data needed to evaluate the conclusions in the paper are present in the paper and/or the Supplementary Materials.

Submitted 10 April 2022
Accepted 1 August 2022
Published 16 September 2022
10.1126/sciadv.abq1677